Materialia 12 (2020) 100764

Contents lists available at ScienceDirect

Materialia

journal homepage: www.elsevier.com/locate/mtla

Full Length Article

Mechanistic insights into the colloidal assembly of mesoporous silica using *in-operando* cross-scale X-ray scattering and spectroscopic measurements

Hassnain Asgar[a], Soenke Seifert[d], Ivan Kuzmenko[d], Michael Bartl[b,c], Greeshma Gadikota[a,*]

[a] School of Civil and Environmental Engineering, Cornell University, Ithaca, NY 14853, United States
[b] Department of Chemistry, University of Utah, Salt Lake City, UT 84112, United States
[c] Center for Energy Efficient Electronics Science, University of California, Berkeley, CA 94720, United States
[d] X-ray Science Division, Advanced Photon Source, Argonne National Laboratory, Lemont, IL 60439, United States

ARTICLE INFO

Keywords:
SBA-15
Mesoporous silica
Salting-in effects
Nitrate
Small-Angle X-ray Scattering
Grazing Incidence-Small Angle X-ray Scattering

ABSTRACT

Advancing a mechanistic understanding of the colloidal to solid-phase transformations of silica allows us to tune these meso-scale structures. In this study, we probe the structural transformations associated with the formation of mesoporous silica particles, SBA-15 using *in-operando* Small Angle X-ray Scattering (SAXS) and Grazing Incidence-Small Angle X-ray Scattering (GI-SAXS). The chemical transformations associated with the hydrolysis and condensation of silica particles is investigated using Attenuated Total Reflection – Fourier Transform Infrared Spectroscopy (ATR-FTIR) measurements. Fast polymerization of Si-O-Si species to form mesoporous silica is noted when SBA-15 is synthesized in the presence of nitrate salts, due to the "salting-in" effect or enhanced solubility of polymers. However, aging the silica particles resulted in plate-like morphologies in the absence of the nitrate salt and spherical morphologies in the presence of nitrate salt. Early onset of nucleation of silica particles in the presence of nitrate salts was captured using GI-SAXS measurements. These studies show that the rational basis for developing new synthesis routes for accelerated kinetics or specific meso-scale structures can be informed by detailed characterization of the evolution in chemistry and meso-scale structure of these materials.

1. Introduction

Developing mechanistic controls on the synthesis of colloidal materials requires us to advance experimental methods to probe the evolution of matter in real-time. Colloidal approaches to synthesize novel materials have gained widespread scientific attention since they allow us to design materials with specific pore and particle morphologies. In particular, the development of siliceous materials via colloidal approaches have received significant attention. Silica is abundant in earth materials and there is an emerging interest in understanding the thermodynamic [1–6] and transport [7–11] behavior of fluids in confinements, especially the Earth's subsurface [12]. To develop a calibrated understanding of anomalous thermodynamic and transport behavior of confined fluids, the development of model materials as surrogates for natural hierarchical materials has been proposed [13,14]. One of the approaches to develop geo-architected siliceous materials is via colloidal synthesis. [15,16]. The morphologies of these ordered mesoporous materials are sensitive to the processing conditions including the temperature and solvent composition [17–21]. Examples of these materials include SBA-15, SBA-16, MCM-41, and MCM-48. These materials can be functionalized for applications in catalysis [22–25], delivery of bioproducts to the body [26,27], and filtration [28–30].

Directing the synthesis of novel materials with specific morphologies requires us to tune the experimental conditions. As an alternative to the conventional route of testing several processing conditions, targeted *in-operando* measurements can reveal important mechanistic insights. Several research efforts have been dedicated to understanding the chemical [31,32] and structural [33–36] changes during the formation of ordered mesoporous silica. Moreover, the effect of electrolytes such as salts [16,37,38], silica precursors [20] and other reagents [21,39,40] and temperature [41] have a significant influence on the morphologies of the silica particles produced via colloidal synthesis.

The synthesis of these materials, when using non-ionic surfactants, is directly controlled by the amphiphilic molecules present in these structure directors or surfactants [21,39]. Amphiphilic molecules used mostly for the ordered mesoporous silica synthesis are the block copolymers such as Pluronic triblock copolymers, which consist of polypropylene (PP) block sandwiched between two polyethylene (PE) blocks [42,43]. In an aqueous solution, Pluronic polymers typically form micelles with a hydrophobic core of polypropylene (PP) block surrounded by a hy-

---

* Corresponding author.
E-mail address: gg464@cornell.edu (G. Gadikota).

https://doi.org/10.1016/j.mtla.2020.100764
Received 1 April 2020; Accepted 30 May 2020

drophilic corona made up of polyethylene (PE) block [43–46]. Water is present as the main part of corona but to some extent, it can also penetrate the core of micelles [45].

It is known that the addition of electrolytes and temperature can affect the properties of Pluronic block copolymers [42,43,47,48]. Moreover, the solubilities of these nonionic block copolymers are influenced by the presence of inorganic salts [16,37,49]. The inorganic salts can either decrease or increase the solubility of organic solutes in the water based on a phenomena termed as the 'salting-out' and 'salting-in' effects, respectively [38]. These effects are primarily governed by the anions in the inorganic salts, while the cations do not have a significant impact. The anions of the Hofmeister series are ordered below in terms of their effect on the solubility of organic solutes; SO_4^{2-}, HPO_4^{2-}, OH^-, F^-, $HCOO^-$, CH_3COO^-, $\mathbf{Cl^-}$, Br^-, NO_3^-, I^-, SCN^-, $ClCO^{4-}$ [16,38,50]. The anions to the left of Cl^- have reduced solubility in macromolecules such as proteins (representing the "salting-out" effect), while those the right represent enhanced solubility (representing the "salting-in" effect), with the influence of Cl^- being ambiguous [16,49,51]. Ions influence the micellar arrangements [45,52,53] leading to different morphologies of mesoporous silica [16,54–56].

The formation of silica particles involves two stages. The first stage involves the formation of micelles containing a hydrophobic core of polypropylene (PP) surrounded by a hydrophilic corona made up of polyethylene (PE). The second stage involves the 2-D hexagonal ordering of the micelles and the formation of silica particles. The reactions below represent the hydrolysis and condensation reactions associated with the formation of mesoporous silica [14,57].

Hydrolysis:

$$\equiv Si\text{-}OC_2H_5 + HO\text{-}H \rightarrow \equiv Si\text{-}OH + C_2H_5OH \qquad \text{Reaction (I)}$$

Water condensation:

$$\equiv Si\text{-}OH + HO\text{-}Si\equiv \;\rightarrow \equiv Si\text{-}O\text{-}Si\equiv + H_2O \qquad \text{Reaction (II)}$$

Alcohol condensation:

$$\equiv Si\text{-}OH + H_5C_2O\text{-}Si\equiv \rightarrow \equiv Si\text{-}O\text{-}Si\equiv + C_2H_5OH \qquad \text{Reaction (III)}$$

Prior *in-situ* Small Angle X-ray Scattering (SANS) studies showed that *in-situ* Small Angle X-ray Scattering (SAXS) studies were modeled to represent the condensation and densification of silica [34]. *In-situ* Small Angle Neutron Scattering (SANS) measurements showed that the salts influence the scattering intensity driven by changes in the composition of the wall [58]. However, some scientific questions remain unanswered. These questions include: (i) How do we delineate the stages that involve the formation of micelles and the 2-D hexagonal ordering of the micelles to form silica particles? (ii) How do these stages vary when considering "salting-in" as an approach to direct the synthesis of colloidal silica? (iii) Does aging the silica particles change the morphology of these materials? To address these questions, we investigated the phenomena that contributes to the densification and condensation of silica using *in-situ* small angle X-ray scattering (SAXS) and Grazing Incidence-Small Angle X-ray Scattering (GI-SAXS). The chemical onset of silica matrix formation was identified using time-dependent ATR-IR measurements. We evaluate the hypothesis that anions that contribute to the "salting-in" effect such as NO_3^- accelerate the densification and condensation of mesoporous silica, SBA-15. Further, we evaluate the influence of aging on the morphology of mesoporous particles. SBA-15 particles have a hexagonal particle shape and a cylindrical pore structure. The influence of nitrate ions on the morphological changes of SBA-15 are probed. These investigations are designed to provide mechanistic insights into the densification and condensation behavior of mesoporous silica via colloidal synthesis.

2. Materials and methods

The reagents used in this study are Pluronic® P123 ($EG_{27}PG_{61}EG_{27}$), tetraethylorthosilicate (TEOS), magnesium nitrate hexahydrate ($Mg(NO_3)_2.6H_2O$) purchased from Sigma Aldrich, and 1 N hydrochloric acid (HCl) acquired from Fisher Scientific. To synthesize SBA-15 particles, 47.74 mL of HCl, 8 g of P123 and 252 mL of water were stirred in a beaker at a rate of 600 rpm and temperature of 313 K. After the complete dissolution of the surfactant, 17 mL of TEOS was added to the solution and mixed for 24 h, followed by filtration and air-drying at 90 °C for 48 h. To investigate the influence of nitrate ions, $Mg(NO_3)_2.6H_2O$ was added to the solution of HCl, P123, and water to achieve a final molarity of 1 M. Therefore, the synthesis step was repeated by adding 17 mL of TEOS to the solution with salt while stirring at 600 rpm and 313 K for 24 h. Throughout this study, we refer to SBA-15 synthesized without the nitrate salt as "M-1" and SBA-15 synthesized with the nitrate salt is referred to as "M-2". To evaluate changes in the chemical bonding during the first 60 min of reaction, infrared (IR) spectra were acquired in an Attenuated Total Reflection (ATR) mode using an Attenuated Total Reflection-Fourier Transform Infrared spectrometer (ATR-FTIR, Nicolet^{TM} iS50, Waltham, MA). Slurry samples with 100 µL in volume were collected every three minutes for the ATR FT-IR analyses. The spectra were collected in the range of 4000–650 cm^{-1} with a total of 32 scans for each run at a resolution of 2 cm^{-1}.

The *in-situ* SAXS measurements were performed to determine the onset of silica matrix formation during the synthesis of mesoporous materials. The synthesis was performed in a beaker as mentioned above and the reaction solution was pumped through a quartz capillary (outer diameter 1.5 mm, thickness 0.2 mm) in a closed-loop system using a peristaltic pump. The schematic of the experimental setup used during the *in-situ* measurements is shown in Fig. S1(a). The pumping rate of solution from solution bath to the capillary was set at 130 mL/min. During the measurements, the beam was centered in the middle of the vertically oriented quartz capillary. The transmission Small Angle X-ray Scattering (SAXS) measurements were performed at sector 9-ID-C at Advanced Photon Source (APS) in Argonne National Laboratory (ANL) [59–66]. The scattering data were acquired within the scattering wave vector (q) range of 0.04–1.6 $Å^{-1}$. q is related to the wavelength (λ) of incident X-ray and the scattering angle (θ) as: $q = (4\pi/\lambda)\sin(\theta/2)$ [67]. X-ray wavelength during the measurements was 0.59 Å, which corresponds to an X-ray energy of 21.0 keV. Total X-ray photon flux received by the instrument was $\sim 10^{13}$ photon mm^{-2} s^{-1} with the beam size of 0.8×0.2 mm. The sample exposure time during each measurement was 30 s. The SAXS instrument was calibrated using silver behenate before the measurements [68]. The 2D data collected by the instrument was reduced to 1D curves, represented as X-ray scattering intensity vs. scattering wave vector (I(q) vs. q($Å^{-1}$)), by using the Nika [69] macro written in the IgorPro software (Wavemetrics, Lake Oswego, OR). The scattering from quartz capillary and respective solutions before the addition of TEOS was subtracted as background from the data. The *in-situ* measurements were performed up to 154 min for each sample. To obtain the detailed insights from the SAXS data, the fitting was performed using the "Small Angle Diffraction" tool in Irena package [70]. The representative modeled curves are shown in Fig. S2.

For the *in-situ* Grazing Incidence-Small Angle X-ray Scattering (GI-SAXS) measurements, the batch reaction assembly was used (Fig. S1(b)). During the GI-SAXS measurements, the mesoporous materials were nucleated on a fused silica substrate. The *in*-situ cell for GI-SAXS measurements has a volume of 6 mL and thus, the amounts of materials added were adjusted accordingly. The description and schematic of the GI-SAXS cell is provided in a prior publication [71]. For instance, 3.94 mL of water, 0.75 mL of HCl, and 0.125 g of P123 were added in the *in*-situ cell and the first measurement was taken without TEOS. In the next step, 0.27 mL of TEOS was injected into the cell through the inlets at the top of the cell. The injection was done remotely using a programmable syringe pump (Hamilton Microlab 600 series). The remote injection assisted us in robust data acquisition without losing any information at the early stage of reaction. The scattering data was acquired for 100 min. The measurements were taken in two steps. In the first step, 50 scans

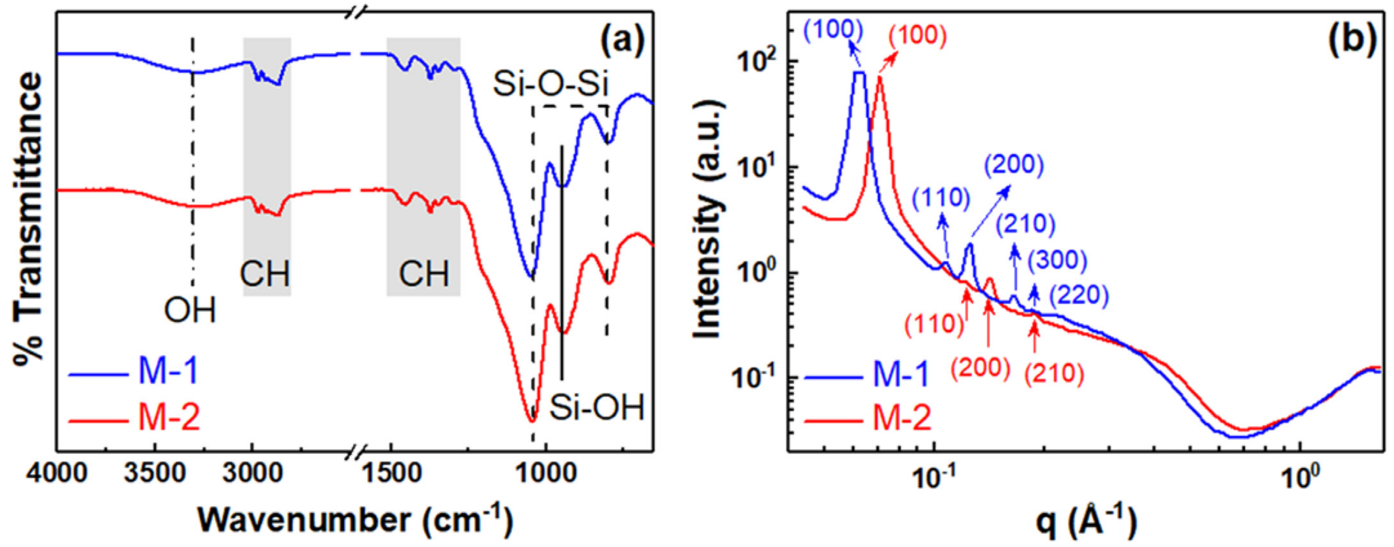

Fig. 1. (a) Identification of the functional groups using Attenuated Total Reflection-Fourier Transform Infrared spectroscopy (ATR-FTIR) measurements, and (b) meso-scale structure determination using Small Angle X-ray Scattering (SAXS) measurements in mesoporous silica, SBA-15 synthesized without (M-1) and with magnesium nitrate salt (M-2).

were taken every 40 s, while in the second step, the interval between each scan was 4 min. The acquisition time for each scan was 1 s. A similar experiment was repeated with the solution bearing the nitrate salt. The GI-SAXS measurements were performed at sector 12 ID-C at APS. The scattered intensity during the measurements was collected on a 2-D Pilatus 2 M detector (Dectris Ltd., Baden, Switzerland). The GI-SAXS instrument was also calibrated for sample-to-detector distance using silver behenate [67]. The sample-to-detector distance during the measurements was 206 cm. The instrument was operated with the X-ray energy of 18 keV, corresponding to the X-ray wavelength of 0.68 Å. The GI-SAXS data were acquired in the q range of 0.006–0.74 Å^{-1}. The X-ray beam was directed to the substrate at an incidence angle (α_i) of 0.11°. The incident angle is lower than the critical angle for total external reflection at the given energy. The GI-SAXS data were cut along the horizontal 433 axis and 1D curves were obtained using an Igor based program.

Finally, the powdered samples synthesized in the laboratory were investigated for pore size and N_2 adsorption-desorption isotherms using the Brunauer–Emmett–Teller technique (BET, Quantachrome NOVA-touch Analyzer, Boynton Beach, FL). To evaluate the chemical species in the final product, the ATR-IR spectra of powders were also collected. The morphologies of particles formed during the syntheses were imaged using a scanning electron microscope (Zeiss LEO 1550 FESEM). These measurements coupled with the *in-situ* X-ray scattering and ATR-FTIR data provided detailed insights into the morphological and chemical evolution of SBA-15 in the presence and absence of the nitrate salt.

3. Results and discussion

3.1. Characterization of SBA-15 particles synthesized with and without the addition of nitrate salt

To evaluate the hypothesis that the chemistry and morphology of SBA-15 particles changes on the addition of nitrate salt, ATR-FTIR spectra and SAXS data of the synthesized M-1 and M-2 powders were collected. These data are shown in Fig. 1(a) and (b), respectively. The functional groups of solid SBA-15 particles remain unchanged when these particles are synthesized with and without the addition of nitrate salt. In the FTIR spectra, the bonds corresponding to Si–O–Si asymmetric, Si–OH, and Si–O–Si symmetric vibrations in the silica matrix are around 1045, 940, and 795 cm^{-1}, respectively [72,73]. Moreover, stretching vibrations from OH bands were noted between 3750 – 3300 cm^{-1}, with additional vibrations from CH bonds from residual surfactant. Detailed assignments to these bands are presented in Table S1. These data show that the chemical composition of SBA-15 particles remains unchanged when the materials are synthesized with and without the nitrate salt (Fig. 1(a)).

Analyses of the SAXS data showed that the characteristic dimensions of SBA-15 change when the material is synthesized using nitrate salt (Fig. 1(b)). The addition of nitrate salt shifted the peak representing the (100) plane to a relatively higher q value of 0.071 Å^{-1} from 0.064 Å^{-1}, which corresponds to the d-spacing of 88.5 Å and 98.2 Å, respectively. The values of all the d-spacings corresponding to labeled peaks are presented in Table S2. The mesoporous lattice types in M-1 and M-2 were evaluated by calculating the ratios of q values of the first four peaks that appeared in the SAXS curves (Fig. 1(b)). The calculated ratios for M-1 and M-2 are presented in Table S3. For both materials, we found that the mesopores were organized as a hexagonal (H_1) lattice [47,48] since both followed ratios of 1: $\sqrt{3}$: $\sqrt{4}$: $\sqrt{7}$. The lattice parameters 'a_0' for M-1 and M-2 were also calculated using the following equation.

$$a_0 = 2 \times d_{(100)}/\sqrt{3} \tag{1}$$

where, $d_{(100)} = 2\pi/q_{(100)}$. The values of 'a' for M-1 and M-2 were found to be 11.64 nm and 10.23 nm, respectively.

Additional insights into the pore sizes were obtained from the BET N_2 adsorption-desorption isotherms, measured at 77 K. The isotherms and pore size distribution of M-1 synthesized in the absence of salt and M-2 synthesized in the presence of nitrate salt are presented in Fig. 2. The pore size distributions for both samples were determined using the BJH method applied to the desorption isotherm. M-1 exhibited a relatively wider pore-size distribution with an average pore diameter of 4.11 nm, while M-2 exhibited a narrow pore-size distribution having an average pore diameter of 3.65 nm (Fig. 2(a)). Moreover, the values of the lattice parameter 'a_0' and average pore size were used to determine the wall thicknesses (a_0 – pore size) in M-1 and M-2 [19]. The pore wall thickness for M-1 and M-2 were found to be 7.5 nm and 6.6 nm, respectively. This decrease in the pore size and thinner walls in the presence of salt can be attributed to the salting-in effect of nitrate ions. The effect of anions on the size of P123 micelles in aqueous solution using small angle X-ray and neutron scattering has been studied by Manet et al., [52] who reported that the anions facilitating salting-out effects produce relatively larger micelles compared to the anions that facilitate the salting-in ef-

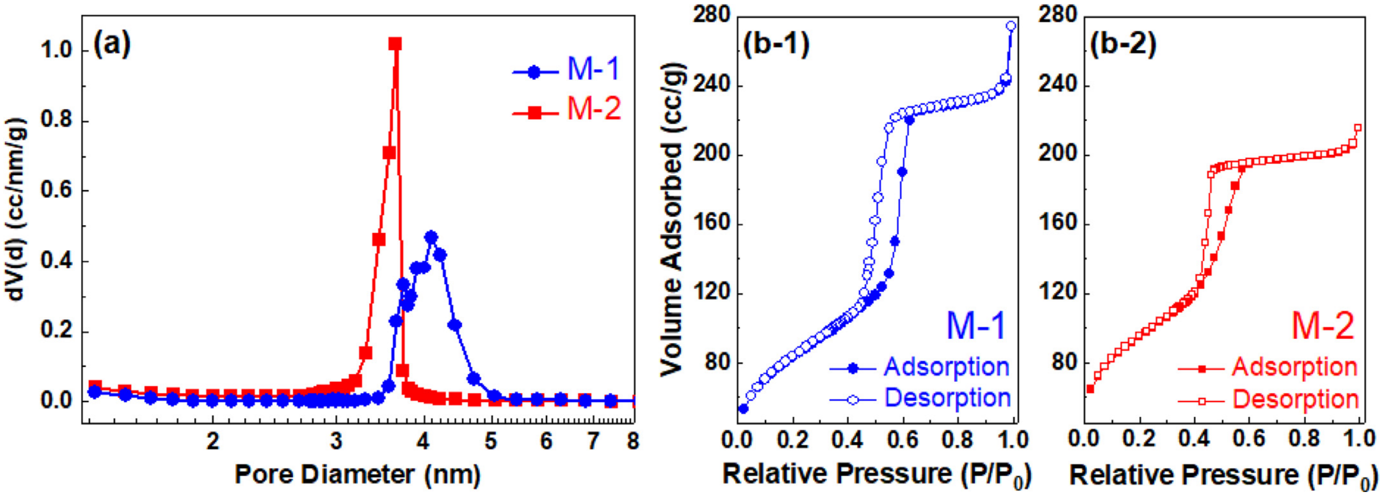

Fig. 2. Pore size distribution curves (a) and N_2 adsorption–desorption isotherms for mesoporous M-1 (b-1) and M-2 (b-2), respectively. M-1 and M-2 represent mesoporous silica, SBA-15 synthesized without and with magnesium nitrate salt.

Table 1
Lattice parameters, pore sizes, wall thicknesses, surface areas, and pore volumes for M-1 and M-2. Lattice parameters were calculated from the first peaks ($q_{(100)}$) in SAXS curves. Pore size distributions, surface area and pore volumes were determined from N_2 adsorption–desorption isotherms. The wall thickness was calculated by subtracting the average pore size from lattice parameter.

Sample ID	Lattice parameter (nm) ($a_0 = \frac{2 \times d_{(100)}}{\sqrt{3}}$)	Pore size (nm) (BJH method)	Wall thickness (nm) ($a_0 - pore\ size$)	Surface area (m^2/g) (BET)	Pore volume (cc/g) (N_2 isotherm)
M-1	11.6	4.1	7.5	375.5	0.44
M-2	10.2	3.6	6.6	370.7	0.33

fects. Since NO_3^- ions facilitate salting in effects, the decrease in the pore size of the final product of M-2 can be attributed to this effect.

The N_2 BET adsorption-desorption isotherms for M-1 and M-2 are presented in Fig. 2(b-1) and (b-2), respectively. Typical type IV-a isotherms were exhibited by both the samples, having a hysteresis which indicates the presence of capillary condensation in the pores [74]. However, the different types of hysteresis loops were presented by both the samples. For instance, M-1 presented a type of H1 hysteresis, which is an indication of uniform mesopores having a delayed condensation on the adsorption branch. For M-2, type H2-(a) hysteresis was noted. This observation is associated with the cavitation-induced evaporation leading to narrower pore size distributions and smaller pores [19,28,74–76] compared to M-1. As evidence, the surface area of M-1 and M-2 are 375.5 m^2/g and 370.7 m^2/g, respectively. The pore volumes of M-1 and M-2 are 0.44 cc/g and 0.33 cc/g, respectively. The pore sizes of M-1 and M-2 are 4.1 nm and 3.6 nm in M-1 and M-2, respectively. These parameters are summarized in Table 1. While the BET pore size measurements showed clear differences in the structure of SBA-15 synthesized with and without the nitrate salt, insights into the evolution of micellular organization leading to the structure of SBA-15 are reported in the following sections.

3.2. *Evolution of the Si-bearing functional groups during the synthesis of SBA-15*

The formation of mesoporous silica is accomplished in two steps [57]. The first step is the hydrolysis of silicate species (TEOS) by water which results in the formation of silanol (Si–OH) as presented by Reaction (I). Following the hydrolysis step is the condensation reaction, which leads to the formation of Si–O–Si linkages, eventually leading to the formation of a well-ordered mesoporous structure. During the condensation reaction, the silanol species react with either another silanol or precursor silicates to form siloxanes (Si–O–Si). The formation of siloxane by the reaction of two silanols is termed as water condensation, while the reaction of silanol with silicates to produce siloxane is called alcohol condensation, as shown in Reactions (II) and (III), respectively.

To capture these chemical changes during the formation of mesoporous M-1 and M-2 materials, the ATR-FTIR measurements were performed as the silica materials were synthesized. For these measurements, 100 μL of the solution was extracted from the reaction mixture and dropped on the ATR diamond crystal for FTIR analyses. The time interval between sample extraction from solution to dropping on ATR crystal was 30 s. Each ATR measurement took approximately 1 min. The time reported here corresponds to the beginning of each measurement. The solutions were well-mixed to ensure that the samples were representative of the solution composition. The FTIR spectra of M-1 and M-2 solutions before the addition of TEOS were taken as the background prior to the measurements. The ATR-FTIR spectra of TEOS, M-1 (pre-TEOS), and M-2 (pre-TEOS) are presented in Fig. S3. The pre-TEOS spectra of M-1 and M-2 were acquired with water as the background. In these IR spectra, the C–O–C and C=O stretching vibrations from Pluronic P123 were observed around ~1090 cm^{-1} and ~1615 cm^{-1}, respectively [77]. For M-2, a peak from asymmetric vibrations of NO_3^- from $Mg(NO_3)_2$ was also noted at 1338 cm^{-1} [78].

During the synthesis, significant changes were noted between 1250 and 850 cm^{-1} in the IR spectra (Fig. 3). Changes for the peaks corresponding to Si–OH (silanol) and Si–O–Si (siloxane) were observed. To understand the underlying chemical transformations, the peaks in the range of 1250–1000 cm^{-1} were deconvoluted to better understand the underlying chemical transformations. This range was selected because the bands corresponding to the final silica product (Si–O–Si) lie within this range as indicated in several literature sources [31,32,79–83]. The deconvoluted spectra at the major representative transformation stages were plotted and shown in Figs. S4 and S5 for M-1, and M-2, respectively. The deconvolution was performed using the Levenberg Marquardt iteration algorithm using the Gauss model embedded

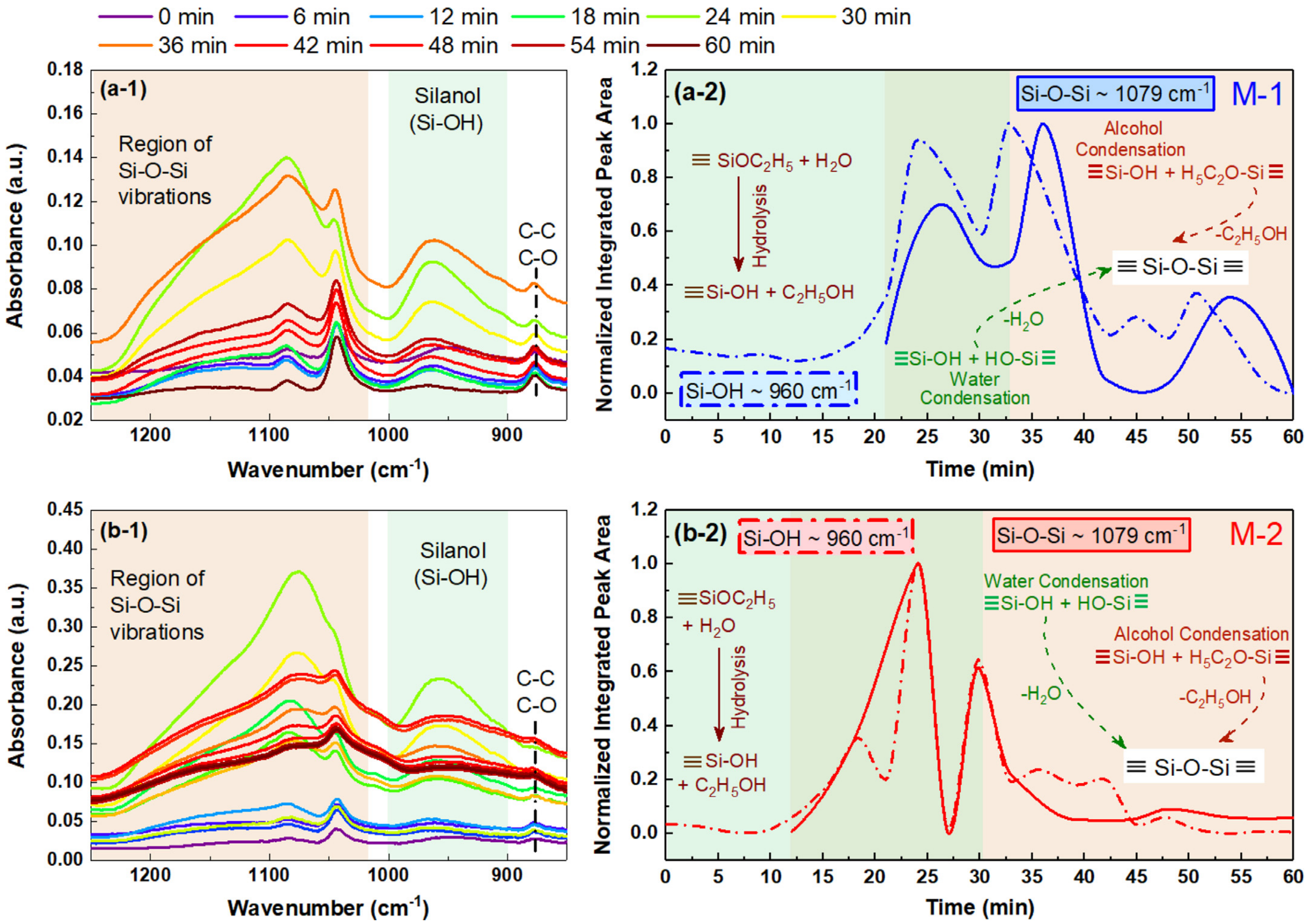

Fig. 3. Evolution of the functional groups during the synthesis of mesoporous silica, SBA-15 in the (a-1) absence (M-1) and (b-1) presence of nitrate ions (M-2). The time evolution of the functional groups based on the normalized integrated peak areas in mesoporous silica, SBA-15 in the (a-2) absence (M-1) and (b-2) presence (M-2) of nitrate ions is shown.

in Origin Pro software (OriginLab Corp.). To compare the evolution of functional groups in both samples, the peaks around ~960 cm^{-1} for Si–OH (silanol) and ~1079 cm^{-1} for Si–O–Si (blue curves in deconvoluted spectra) in silica matrix were selected. Although multiple Si–O–Si vibration modes were identified during the peak deconvolution, the bands around 1079 cm^{-1} were selected as representative bands for siloxane vibrations. The integrated peak areas for Si-OH (~960 cm^{-1}) and Si–O–Si (~1079 cm^{-1}) were determined and the values were normalized by the maximum value. The normalized integrated peak areas for Si–OH and Si–O–Si are plotted in Fig. 3(a-2) and (b-2) for M-1 and M-2, respectively. In M-1, the C–O and C–C peaks from ethanol were observed in the first scan (0 min) shown in Fig. S4(a), which is an indication of hydrolysis of silicate species by water. Similar behavior was exhibited by M-2 at 0 min, as presented in Fig. S5(a). Moreover, the actual integrated peak areas and associated errors for peaks around ~1079 cm^{-1} are shown in Fig. S6.

Our hypothesis when analyzing the ATR-FTIR data was that the trends in the absorbance vary as transformations from the colloidal to solid phase occur, which was confirmed based on the data presented in Fig. 3. Deconvolution of Si–O–Si peaks provided insights into the mechanisms governing the formation of silica particles. The first peak for Si–O–Si (~1079 cm^{-1}) was noted after 21 min for M-1, while for M-2 it was noted after 12 min. Si–O–Si bands (~1079 cm^{-1}) followed a similar trend as Si–OH band (~960 cm^{-1}), which corresponds to the simultaneous hydrolysis of TEOS and condensation of silanol (Si–OH) to produce siloxane (Si–O–Si) linkages in the mesoporous silica matrix. The downward trend in the integrated peak area curves was attributed to the separation of precipitated particles from the solution phase, with the solvent in contact with the ATR crystal. Further, additional vibration modes for Si–O–Si were also identified in the deconvoluted spectra of both M-1 (Fig. S4) and M-2 (Fig. S5). These peaks could be attributed to the co-existence of different internal and external Si–O vibrations between 1200 and 1000 cm^{-1}, which has been reported to exist during the formation of mesoporous MCM-41 [31]. Additionally, the asymmetric Si–O band from unreacted TEOS was also noted for both the samples, which shifted from ~1125 cm^{-1} (0 min) to ~1200 cm^{-1} during the formation of the mesoporous matrix.

The ATR-IR measurements have shown that in the presence of nitrate anions, the onset of siloxane formation was relatively early (12 min) when compared with the solution (21 min) without salt. This observation is consistent with the hypothesis that anions that facilitate "salting in" effects enabling higher solubility of the polymers and early onset of micellization [38,52]. These studies show that early micellization facilitated by nitrate ions enables the early onset of hydrolysis and condensation of the silica matrix, as noted for M-2. To compliment these spectroscopic investigations which provide insights into the dynamic chemical evolution of colloidal silica material systems leading to the formation of mesoporous silica, *in-operando* evolution in the meso-scale features of silica with and without nitrate salts is probed using Small Angle X-ray Scattering (SAXS) and Grazing Incidence-Small Angle X-ray Scattering (GI-SAXS) measurements, as discussed in the following sections.

3.3. Dynamic evolution in the meso-scale features of silica

To monitor the evolution of mesoporous phase formation, *in-situ* SAXS measurements were performed in transmission and grazing incidence geometries. The *in-situ* transmission SAXS curves for M-1 and M-2 are presented in Fig. 4(a) and (b), respectively. The increase in the scattering intensity in case of M-2 could be referred to the increase in scattering length density (SLD) in the presence of $Mg(NO_3)_2$ (SLD = 19.47×10^{-6} Å^{-2}). The integrated intensities of both samples were also calculated and plotted in Fig. 4(c) for M-1 and M-2, respectively. The peaks and Guinier knee-like feature around 0.3 Å^{-1} were fitted using the 'small angle diffraction' tool using the *Irena* program [70] in *IgorPro* software. The SAXS data for M-1 and M-2 were interpreted using hexagonal close-packed (HCP) cylindrical geometry, which is consistent with the meso-scale organization of these materials [47,48]. However, the Guinier knee was fitted using the approach proposed by Beaucage [84,85]. The model was fitted between the q values of 0.2–0.8 Å^{-1} to obtain the radius of gyration (R_g) values, which are reported in Fig. 5.

Important insights into the evolution of the meso-scale features of silica can be obtained by investigating changes in the (100) characteristic peak which corresponds to the ordered mesopores [16,19,34]. Further, the intensity of (100) characteristic peak was observed to be increasing with time as the mesoporous silica phase was formed. In the case of M-1, the onset of the (100) peak at 25 min (Fig. 4(a)) corresponded to the onset of siloxane formation, as discussed in Section 3.2. In the case of M-2 in which the SBA-15 is synthesized in the presence of nitrate salt, the characteristic peak was noted as early as 2 min. The earlier development of the (100) peak in mesoporous silica synthesized using the nitrate salt, M-2 (Fig. 4(b)) [86] is consistent with the earlier onset of siloxane linkages noted in Section 3.2.

To determine whether the scattering was from micelles or mesoporous phase, the values of d-spacing corresponding to the peak centers were analyzed. For M-1, initially, the d-spacing of 11.0 nm was observed, which could be attributed to the scattering from micelles in the solution. Comparable values of d-spacing for P123 micelles have been reported in the literature [16,86]. At the onset of siloxane (Si–O–Si) condensation (~27 min), the d-spacing value decreased to 10.4 nm and remained constant until 83 min of reaction. After 83 min of reaction, the d-spacing value changed to 9.9 nm and remained constant until the end of SAXS measurements. This decrease in d-spacing is attributed to the densification of silica-phase around the micelles [21,58,87,88]. For M-2, in which nitrate ions were present in the solution, the d-spacing values for (100) plane exhibited a similar trend as shown by M-1. However, the initial value (13.5 nm) was relatively higher than the M-1. The first decrease in the d-spacing value was noted after 10 min, where the value decreased from 13.5 to 12.5 nm and eventually attained a value of 11.7 nm after 18 min. Upon further reaction for up to 50 min, the d-spacing value decreased to 11.0 nm and remained constant until 75 min. Afterward, the values changed to 10.4 nm and remained constant until the end of the reaction.

The d-spacing of M1 determined from the *in-situ* measurements and *ex-situ* measurements of the synthesized powder was 9.9 nm and 9.8 nm, respectively. These data are in reasonable agreement with each other. The d-spacing of M2 synthesized with nitrate salt from the *in-situ* measurements and ex-situ measurements of the synthesized sample was 10.4 nm and 8.9 nm, respectively. The discrepancy in these data is attributed to the influence of aging these samples on the changes in the mesoscale structure. To probe the effect of aging on the morphology of the particles, SEM images were taken (Fig. 6).

The micro-scale morphology of M-1 and M-2 particles was also imaged using SEM and presented in Fig. 6(a-1) and (b-1), respectively. The observed morphology of SBA-15 particles synthesized at room temperature (Fig. 6(a-1)) is consistent with the observations from prior publications [19,21]. However, when nitrate ions were present in the solution (Fig. 6(b-1)), no regular morphology was observed. The morphologies of

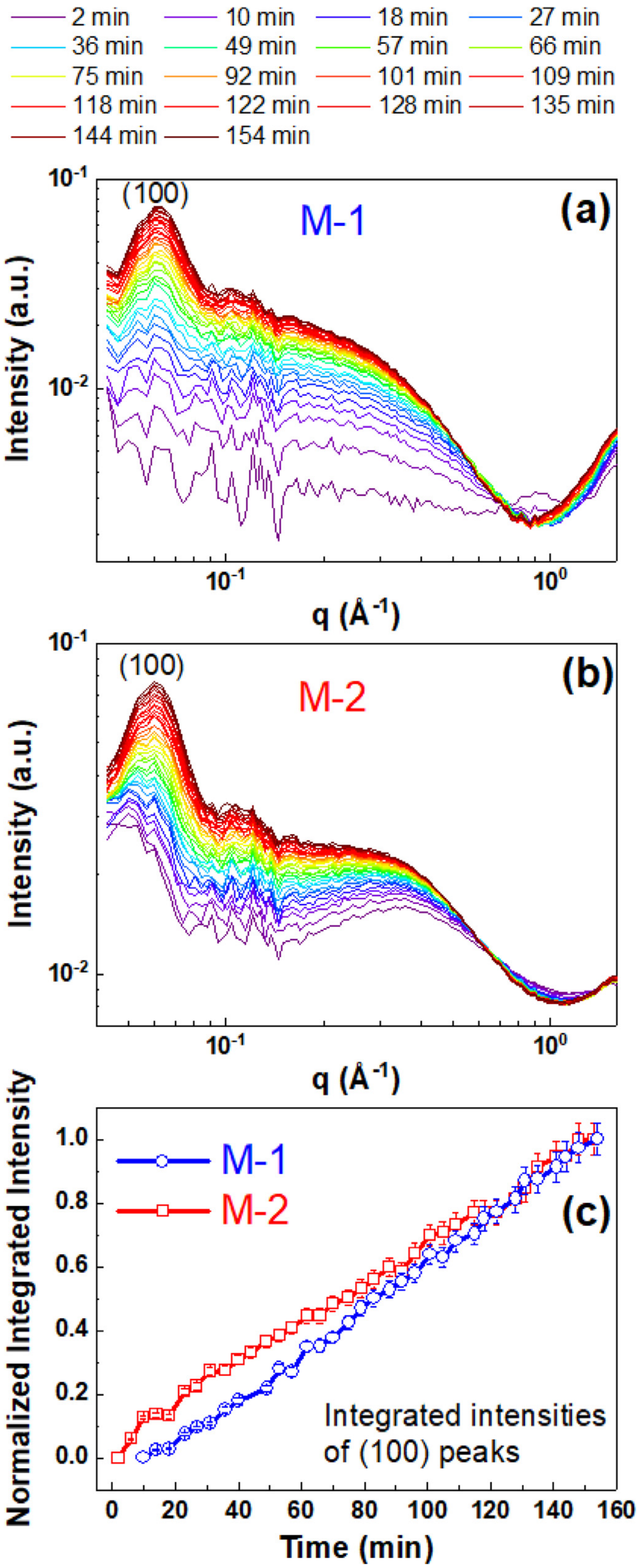

Fig. 4. Evolution in the characteristic *d* (100) peak in mesoporous silica, SBA-15 synthesized in the (a) absence (M-1) and (b) presence (M-2) of nitrate salt using *in-operando* Small Angle X-ray Scattering (SAXS) measurements. Comparison of the normalized integrated peak intensity of the *d* (100) peak is shown in **(c)**.

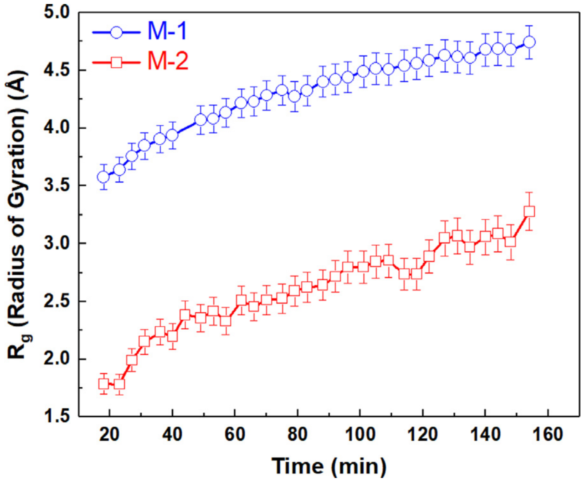

Fig. 5. Estimated radius of gyration (Rg) values for M-1 and M-2 between the q-range of 0.2–0.8 Å-1 obtained from the transmission SAXS measurements.

synthesized silica particles have been shown to be sensitive to temperature [41]. Prior literature suggested that Cl^- ions result in well-defined and regular particle morphologies, Br^- ions yield small and slightly irregular particle morphologies while I^- ions do not result in regular morphologies [16]. In the Hofmeister series for evaluating salting-in effects, nitrate is located in between Br^- and I^- ions. The initial irregular morphologies observed when using I^- ions to synthesize silica particles [16] is consistent with that of nitrate ions in this study. However, we observed that aging the samples synthesized in nitrate salts, changes the particle morphology. SEM images were collected on samples aged for two weeks at room temperature under static conditions (Fig. 6(a-2) and (b-2)). Aging M-1 samples prepared in the absence of nitrate salts resulted in platelet or disk-like morphology (Fig. 6(a-2)). However, in the presence of nitrate ions, the random particles initially formed were transformed into spherical particles (Fig. 6(b-2)). The particle size was also found to be increased in both cases, which was a direct effect of aging in the solution, as reported previously [89].

The formation of spherical particles in M-2 could be attributed to the intrinsic need of the system to minimize the surface energy [90]. It has been reported that in the presence of salt, more water is expelled during the synthesis resulting in a more flexible molecular rearrangement and thermodynamically favorable structures [16,91]. Therefore, the presence of NO_3^- ions in the solution, could help minimize the surface energy and eventually produce particles with spherical morphologies. Additionally, if the polymerization of inorganic species (Si–O–Si) is slow relative to the formation of the meso-structure, then well-defined mesostructured materials are developed. However, irregular particles are formed if inorganic species polymerize relatively fast [16,90]. Therefore, to understand whether the spherical morphology of M-2 particles was controlled by the presence of NO_3^- ions or aging in the solution where the existing silica phase might influence

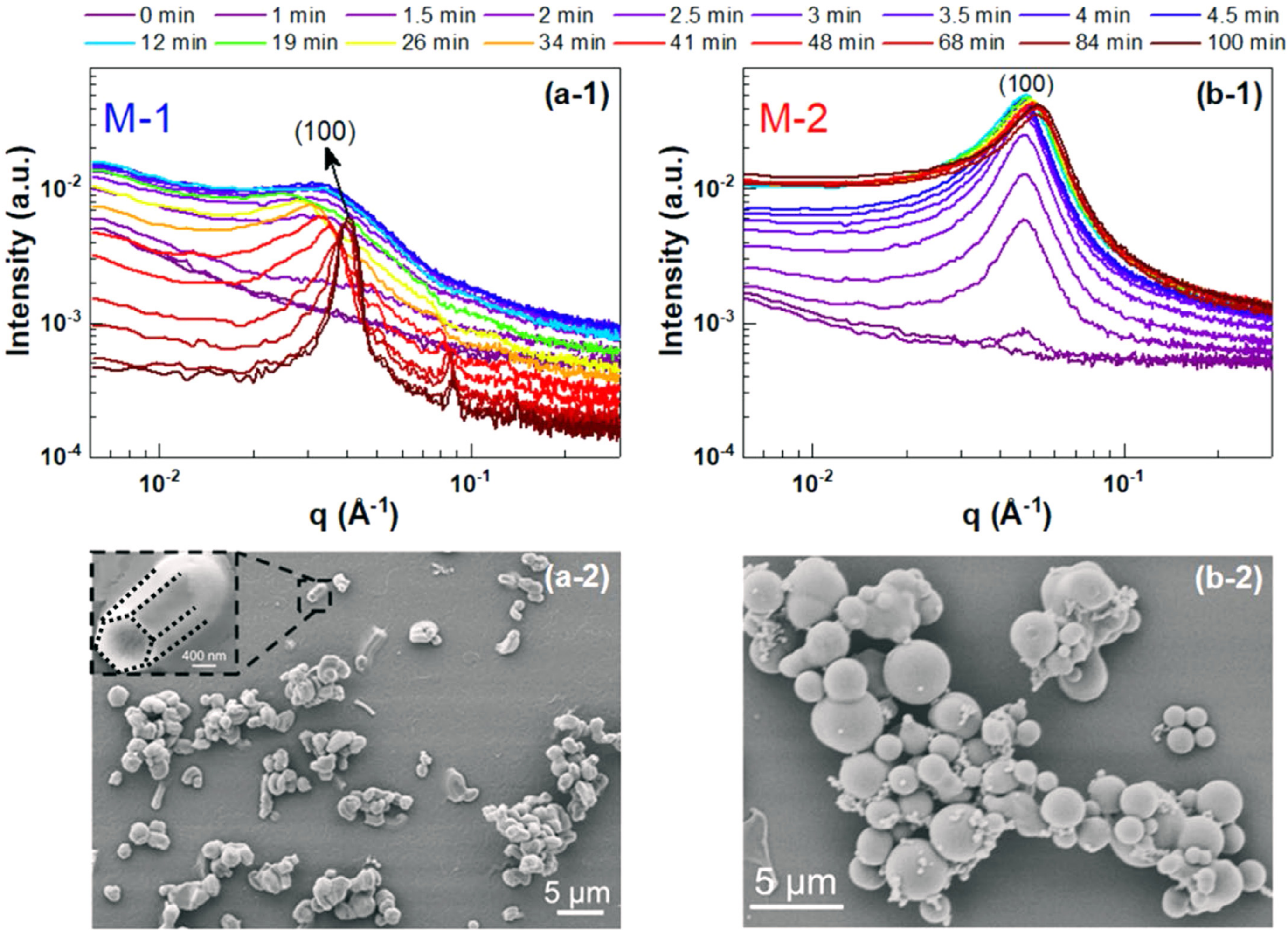

Fig. 6. Morphologies of as-prepared (a-1) M-1 and (b-1) M-2 and, (a-2) M-1 and (b-2) M-2 aged for three weeks represented using Scanning electron micrographs (SEM). M-1 and M-2 represent mesoporous silica, SBA-15 synthesized without and with magnesium nitrate salt.

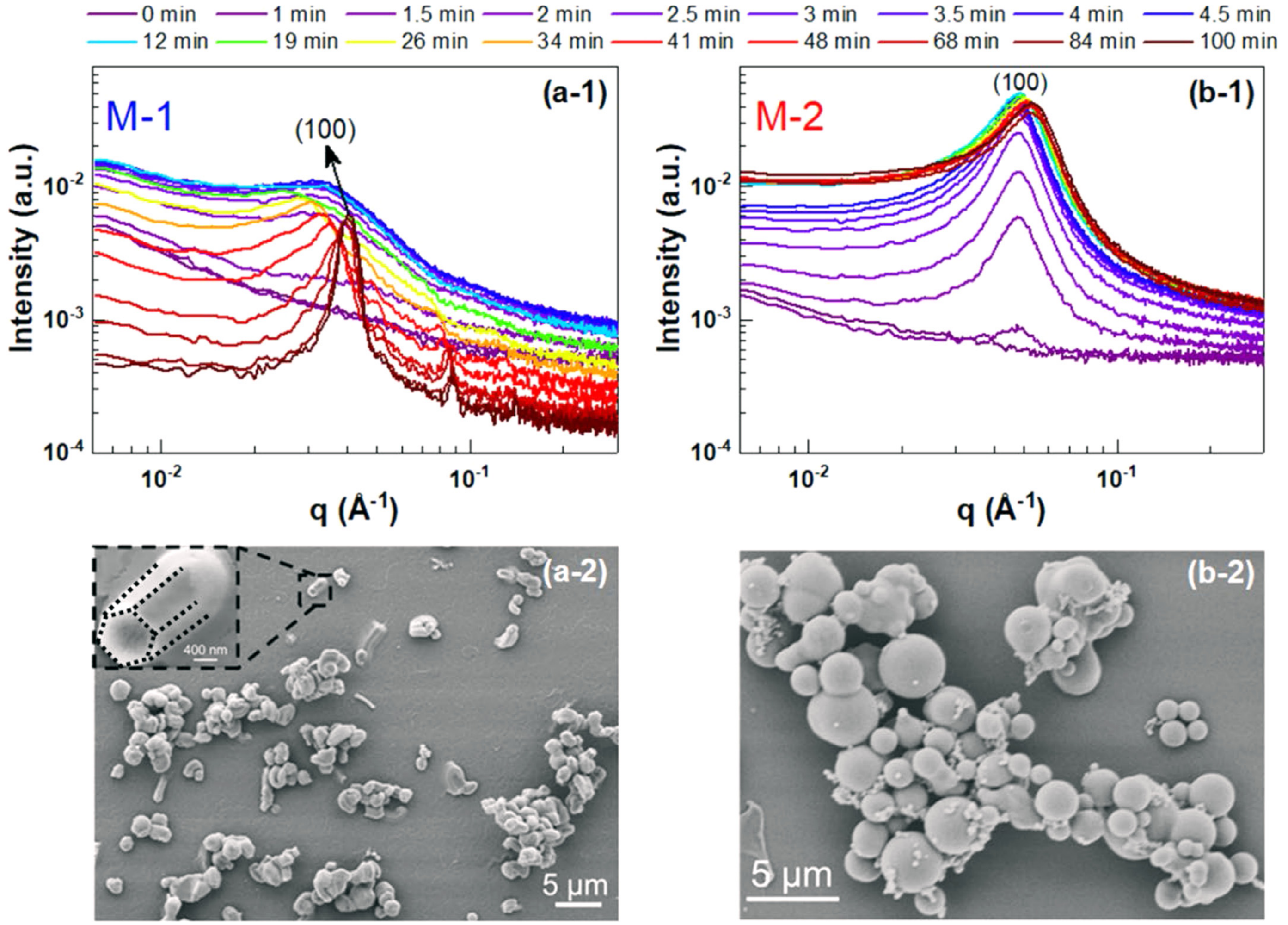

Fig. 7. Evolution in the characteristic *d* (100) peak in mesoporous silica, SBA-15 synthesized in the (a-1) absence (M-1) and (b-1) presence (M-2) of nitrate salt using *in-operando* Grazing Incidence-Small Angle X-ray Scattering (GI-SAXS) measurements. The morphologies of (a-2) M-1 and (b-2) M-2 are captured using Scanning electron micrographs (SEM).

the final morphology, the SAXS experiments were repeated in a GI-SAXS geometry and the mesoporous particles were precipitated on fused silica-substrates.

To understand the effect of the substrate or existing silica phase on the morphology of mesoporous particles, *in-situ* GI-SAXS measurements were performed, as described in Section 2. Briefly, 3.94 mL of water, 0.75 mL of HCl, and 0.125 g of P123 were added in the cell followed by injection of 0.27 mL of TEOS after the first measurements. The evolution of (100) characteristic peaks for both M-1 and M-2 are presented in Fig. 7(a-1) and (b-1), respectively. It can be noted that the (100) peak appears after 26 min for M-1 (Fig. 7(a-1)), which is relatively late when compared with the emergence of (100) peak in M-2 (Fig. 7(b-1)). In the case of M-2, the small peak was noted for the curve at 1 min, however, a prominent peak at 1.5 min was observed. These data show that the presence of nitrate ions facilitates the early nucleation of silica particles.

Scattering from M-1 showed that a broad peak appeared after 12 min. This peak was attributed to the scattering from the micelles formed and accumulated at the substrate. The initial data from micelles for M-1 was fitted using the core-shell model available in *Irena* program [70] and presented in Fig. S7. Additionally, the parameters calculated from the model fitting are reported in Table S4. The d-spacing value for M-1 at 12 min was noted to be 25.2 nm, which decreased to 18.8 nm after 33 minutes, where the first sharp peak was observed. This decrease in the d-spacing value can be attributed to the densification of silica-phase around the micelles as a result of Si–O–Si polymerization, which increases X-rays contrast. Finally, the d-spacing value decreased to 15.4 nm after 100 minutes of reaction. In the case of M-2, a significant (100) peak from micelles/mesostructures was noted just after two minutes and an increase in the peak growth was observed. Initially, for M-2, the d-spacing of 13.2 nm was observed at 2 min. However, as the reaction proceeded, d-spacing decreased from 12.7 nm at 17 min to 11.9 nm after 100 min. Additionally, the full width half maximum (FWHM) of (100) peaks for M-1 and M-2 were also calculated and are presented in Fig. S8(a) and (b), respectively. After 33 min of reaction times, FWHM values for M-1 started to decrease and achieved a constant value after 60 min. However, in the case of M-2, the FWHM value slightly increased due to peak broadening and achieved a relatively constant value at a comparatively early stage (~12 min). These findings were similar to those noted in ATR-IR and transmission SAXS measurements, where Si–O–Si polymerization and pore densification were noted after 25–27 min for M-1 and 10–12 min for M-2.

The SEM images of M-1 and M-2 particles nucleated on the fused silica substrates during GI-SAXS measurements were also acquired to analyze the micron-scale morphology. The SEM images are presented in Fig. 6(a-2) and (b-2), respectively. For M-1, hexagonal and cylindrical morphologies were observed as noted in the as-synthesized sample (Fig. 6(a-1)). However, upon addition of nitrate ions, spherical mesoporous particles were formed (Fig. 6(b-2)). The formation of spherical particles in the case of M-2 can be related to the influence of the existing silica substrate which assists the NO_3^- ions to lower the surface energy during

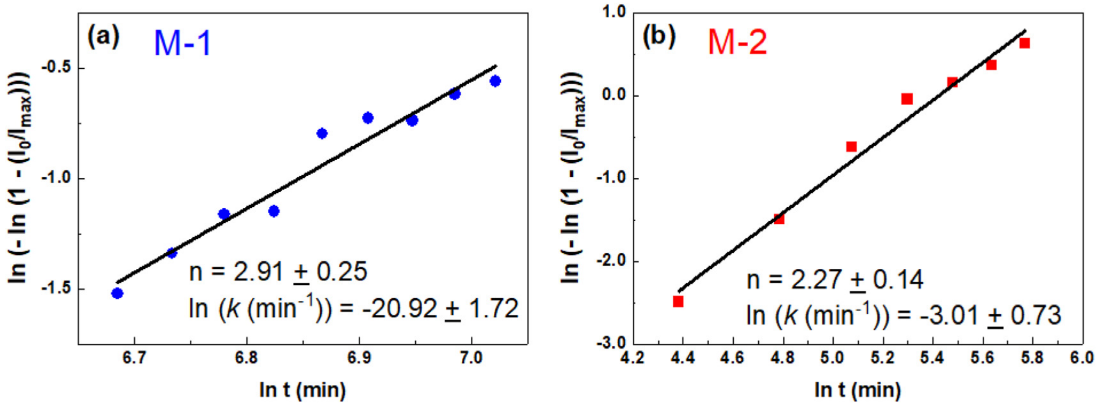

Fig. 8. Avrami plots for (a) M-1 and (b) M-2 determined from GI-SAXS data. M-1 and M-2 represent mesoporous silica, SBA-15 synthesized without and with magnesium nitrate salt, respectively.

the relatively fast polymerization of Si–O–Si in mesostructure formation [90]. Further information about the kinetics of mesostructure development was obtained from the GI-SAXS data by fitting the (100) peak intensity vs. time data to the Avrami equation. The Avrami equation can be used to obtain insights into the phase transformation processes involving continuous nucleation, loss or gain of a phase [92–95]. The mathematical expression for the Avrami equation is represented below:

$$X_s(t) = 1 - e^{-kt^n} \tag{2}$$

where, $X_s(t) = I_s(t)/I_s(\infty)$, is the fraction of mesostructure formed at time *t*, *n* is the Avrami index, and *k* is the rate coefficient. The value of $X_s(t)$ was calculated by dividing the intensity of (100) peak by the maximum observed intensity. The Avrami equation can be modified into a linearized form by re-writing as follows:

$$\ln\left(\ln\left[1 - X_s(t)\right]\right) = n\ ln\ t + ln\ k \tag{3}$$

The fits performed on linearized Avrami equation, and parameters obtained are presented in Fig. 8, and Table 1, respectively. The Avrami index reflects the nature of transformation and corresponds to the mechanism of crystal growth or, in the present case, the formation of silica mesostructure [92,96,97]. The value of $n = 1$ corresponds to the one-dimensional (1-D) growth of the objects, $n = 2$ is attributed to the two-dimensional (2-D) growth with the nucleation at the start of process, while $n = 3$ presents the three-dimensional (3-D) growth of instantaneously formed nuclei or 2-D growth at a constant nucleation rate [92]. In the case of M-1, the onset of (001) peak is 26 min. Fitting the data in the time scales of 13–20 min, just before the appearance of mesostructured phase, gives an Avrami index, *n* of 2.91 ± 0.25, corresponding to 2-D growth at a constant nucleation rate (Fig. 8(a)). In the case of M-2, the onset of nucleation is 1.5 min. After 6 min, densification of silica particles is noted. Fitting the data in the range of 1.3–5.3 min results in a *n* value of 2.27 ± 0.14. The GI-SAXS data together with transmission SAXS and ATR-FTIR data facilitate mechanistic insights into the colloidal assembly of mesoporous silica and guide future synthesis efforts.

4. Conclusions

Elucidating the reaction mechanisms, the compositions and chemistry of the reactants on the meso-scale morphologies of silica synthesized via colloidal pathways is essential for developing mechanistic insights into these pathways. In this study, we describe the chemical transformations underlying the hydrolysis and condensation of silica species in the presence and absence of nitrate ions as determined using time-resolved ATR FT-IR measurements. Fast polymerization of Si-O-Si species to form mesoporous silica is noted when SBA-15 is synthesized in the presence of nitrate salts. Transmission SAXS measurements showed that the onset of 2-D hexagonal structure is accelerated in the presence of nitrate salts. However, the equilibrium meso-scale structure is influenced by aging in the synthesis solution, resulting in plate-like morphologies in the absence of the nitrate salt and spherical morphologies in the presence of nitrate salt after two weeks. Further, GI-SAXS measurements show the early nucleation of silica particles when synthesized from solutions bearing nitrate salt. These studies show that tuning the reaction conditions to achieve specific meso-scale morphologies can be informed by characterizing the dynamic evolution in the meso-scale structure of silica.

Supporting Information: Tables summarizing the ATR-IR functional groups, SAXS parameters, ratios of *q* values observed in SAXS of as-synthesized powders, and parameters calculated from scattering of micelles using core-shell model. Schematic of experimental setup during *in-situ* X-ray scattering measurements. Plots of fitted models for transmission SAXS measurements. ATR-IR spectra of precursors. Deconvoluted ATR-IR peaks during the synthesis of M-1 and M-2 in the range of 1250–1000 cm^{-1}. Integrated peak areas for Si–O–Si (~1079 cm^{-1}) of M-1 and M-2. Plots of fitted model for micelle scattering in M-1. FWHM curves for M-1 and M-2 calculated from *in-situ* GI-SAXS curves.

Declaration of Competing Interest

The authors declare that they have no known competing financial interests or personal relationships that could have appeared to influence the work reported in this paper.

Acknowledgments

This work was supported as part of the EFRC-MUSE, an Energy Frontier Research Center funded by the U.S. Department of Energy, Office of Science, Basic Energy Sciences under Award #DE-SC0019285. Hassnain Asgar would like to acknowledge the help provided by Dr. Jan Ilavsky during the data analysis, X-ray Science Division, Argonne National Laboratory. The use of the Advanced Photon Source, an Office of the Science User Facility operated for the U.S. Department of Energy (DOE) Office of Science by Argonne National Laboratory, is supported by the U.S. DOE under Contract DE-AC02-06CH11357. This work made use of the electron microscopy facility of the Cornell Center for Materials Research (CCMR) #DMR-1719875 with support from the National Science Foundation Materials Research Science and Engineering Centers (MRSEC) program (DMR 1120296).

Supplementary materials

Supplementary material associated with this article can be found, in the online version, at doi:10.1016/j.mtla.2020.100764.

References

[1] H. Cho, D. Caputo, M.H. Bartl, M. Deo, Measurements of hydrocarbon bubble points in synthesized mesoporous siliceous monoliths, Chem. Eng. Sci. 177 (2018) 481–490, doi:10.1016/j.ces.2017.12.005.

[2] H. Cho, M.H. Bartl, M. Deo, Bubble point measurements of hydrocarbon mixtures in mesoporous media, Energy Fuels 31 (2017) 3436–3444, doi:10.1021/acs.energyfuels.6b02424.

[3] Z. Jin, A. Firoozabadi, Phase behavior and flow in shale nanopores from molecular simulations, Fluid Phase Equilib. 430 (2016) 156–168, doi:10.1016/j.fluid.2016.09.011.

[4] P. Kumar, S.V Buldyrev, F.W. Starr, N. Giovambattista, H.E. Stanley, Thermodynamics, structure, and dynamics of water confined between hydrophobic plates, Phys. Rev. E 72 (2005) 051503, doi:10.1103/PhysRevE.72.051503.

[5] M. Alfi, H. Nasrabadi, D. Banerjee, Experimental investigation of confinement effect on phase behavior of hexane, heptane and octane using lab-on-a-chip technology, Fluid Phase Equilib. 423 (2016) 25–33, doi:10.1016/j.fluid.2016.04.017.

[6] T. Le, A. Striolo, C.H. Turner, D.R. Cole, Confinement effects on carbon dioxide methanation: a novel mechanism for abiotic methane formation, Sci. Rep. 7 (2017) 9021, doi:10.1038/s41598-017-09445-1.

[7] C. Iacob, J.R. Sangoro, W.K. Kipnusu, R. Valiullin, J. Karger, F. Kremer, Enhanced charge transport in nano-confined ionic liquids, Soft Matter 8 (2012) 289–293, doi:10.1039/c1sm06581e.

[8] Y. Liu, Q. Wang, T. Wu, L. Zhang, Fluid structure and transport properties of water inside carbon nanotubes, J. Chem. Phys. 123 (2005) 234701, doi:10.1063/1.2131070.

[9] Y. Liu, Q. Wang, L. Lu, Transport properties and distribution of water molecules confined in hydrophobic nanopores and nanoslits, Langmuir 20 (2004) 6921–6926, doi:10.1021/la036325l.

[10] Y. Zhang, W. Yu, K. Sepehrnoori, Y. Di, Investigation of nanopore confinement on fluid flow in tight reservoirs, J. Pet. Sci. Eng. 150 (2017) 265–271, doi:10.1016/j.petrol.2016.11.005.

[11] T. Xu, J.A. Apps, K. Pruess, Reactive geochemical transport simulation to study mineral trapping for CO_2 disposal in deep arenaceous formations, J. Geophys. Res. 108 (2003) 2071, doi:10.1029/2002JB001979.

[12] L.J. Pyrak-Nolte, D.J. DePaolo, T. Pietraß, Controlling Subsurface Fractures and Fluid Flow: A Basic Research Agenda Report of a Roundtable Convened to Consider Foundational Research Relevant to Subsurface Technology and Eng, Germantown, MD, 2015.

[13] J. De Yoreo, D. Mandrus, L. Soderholm, Basic Research Needs for Synthesis Science: Report of the Basic Energy Sciences Workshop on Basic Research Needs for Synthesis Science for Energy Relevant Technology, 2016.

[14] H. Asgar, V. Semeykina, M. Hunt, S. Mohammed, I. Kuzmenko, I. Zharov, G. Gadikota, Thermally-induced morphological evolution of spherical silica nanoparticles using *in-operando* x-ray scattering measurements, Colloids Surf. A Physicochem. Eng. Asp. (2019) 124260, doi:10.1016/j.colsurfa.2019.124260.

[15] D. Zhao, J. Sun, Q. Li, G.D. Stucky, Morphological control of highly ordered mesoporous silica SBA-15, Chem. Mater. 12 (2000) 275–279, doi:10.1021/cm9911363.

[16] C.V. Teixeira, H. Amenitsch, P. Linton, M. Lindén, V. Alfredsson, The role played by salts in the formation of SBA-15, an *in-situ* small-angle X-ray scattering/diffraction study, Langmuir 27 (2011) 7121–7131, doi:10.1021/la1043798.

[17] C. Pirez, J.C. Morin, J.C. Manayil, A.F. Lee, K. Wilson, Sol-gel synthesis of SBA-15: impact of HCl on surface chemistry, Microporous Mesoporous Mater. 271 (2018) 196–202, doi:10.1016/j.micromeso.2018.05.043.

[18] X. Wang, Y. Zhang, W. Luo, A.A. Elzatahry, X. Cheng, A. Alghamdi, A.M. Abdullah, Y. Deng, D. Zhao, Synthesis of ordered mesoporous silica with tunable morphologies and pore sizes via a nonpolar solvent-assisted Stöber method, Chem. Mater. 28 (2016) 2356–2362.

[19] D. Zhao, J. Feng, Q. Huo, N. Melosh, G.H. Fredrickson, B.F. Chmelka, G.D. Stucky, Triblock copolymer syntheses of mesoporous silica with periodic 50 to 300 angstrom pores, Science 279 (1998) 548–552, doi:10.1126/science.279.5350.548.

[20] T. Kjellman, V. Alfredsson, The use of *in-situ* and *ex-situ* techniques for the study of the formation mechanism of mesoporous silica formed with non-ionic triblock copolymers, Chem. Soc. Rev. 42 (2013) 3777–3791, doi:10.1039/c2cs35298b.

[21] J.L. Blin, M. Impéror-Clerc, Mechanism of Self-Assembly in the synthesis of silica mesoporous materials: *in-situ* studies by X-ray and neutron scattering, Chem. Soc. Rev. 42 (2013) 4071–4082, doi:10.1039/c2cs35362h.

[22] H. Takahashi, B. Li, T. Sasaki, C. Miyazaki, T. Kajino, S. Inagaki, Immobilized enzymes in ordered mesoporous silica materials and improvement of their stability and catalytic activity in an organic solvent, Microporous Mesoporous Mater 44–45 (2001) 755–762.

[23] B. Rac, A. Molnar, P. Forgo, M. Mohai, I. Bertoti, A comparative study of solid sulfonic acid catalysts based on various ordered mesoporous silica materials, J. Mol. Catal. A Chem. 244 (2006) 46–57, doi:10.1016/j.molcata.2005.08.043.

[24] J. Requies, M.B. Güemez, P.L. Arias, Pore size tuning of functionalized SBA-15 catalysts for the selective production of furfural from xylose, Appl. Catal. B Environ. 115–116 (2012) 169–178, doi:10.1016/j.apcatb.2011.12.025.

[25] A. Taguchi, F. Schu, Ordered mesoporous materials in catalysis, Microporous Mesoporous Mater. 77 (2005) 1–45, doi:10.1016/j.micromeso.2004.06.030.

[26] P. Yang, S. Gai, J. Lin, Functionalized mesoporous silica materials for controlled drug delivery, Chem. Soc. Rev. 41 (2012) 3679–3698, doi:10.1039/c2cs15308d.

[27] I.I. Slowing, J.L. Vivero-escoto, C. Wu, V.S. Lin, Mesoporous silica nanoparticles as controlled release drug delivery and gene transfection carriers, Adv. Drug Deliv. Rev. 60 (2008) 1278–1288, doi:10.1016/j.addr.2008.03.012.

[28] J. Jammaer, T.S. Van Erp, A. Aerts, C.E.A. Kirschhock, J.A. Martens, Continuous synthesis process of hexagonal nanoplates of p6m ordered mesoporous silica, J. Am. Chem. Soc. 133 (2011) 13737–13745, doi:10.1021/ja205627t.

[29] Y. Ye, G. Liang, B. Chen, W. Shen, C. Tseng, M. Cheng, J. Rick, Y. Huang, F. Chang, B. Hwang, Effect of morphology of mesoporous silica on characterization of protic ionic liquid-based composite membranes, J. Power Sources 196 (2011) 5408–5415, doi:10.1016/j.jpowsour.2011.02.066.

[30] A. Alvarez, C. Guzmán, A. Carbone, A. Saccà, I. Gatto, R. Pedicini, E. Passalacqua, R. Nava, R. Ornelas, J. Ledesma-garcía, L.G. Arriaga, Composite membranes based on micro and mesostructured silica: a comparison of physicochemical and transport properties, J. Power Sour. 196 (2011) 5394–5401, doi:10.1016/j.jpowsour.2011.02.072.

[31] S.M. Holmes, V.L. Zholobenko, A. Thursðeld, R.J. Plaisted, C.S. Cundy, J. Dwyer, In-situ FTIR Study of the Formation of MCM-41, J. Chem. Soc., Faraday Trans. 94 (1998) 2025–2032.

[32] V.R. Koganti, S. Das, S.E. Rankin, In-situ FTIR Investigation of the Kinetics of Silica Polycondensation in Surfactant Templated Mesostructured Thin Films, J. Phys. Chem. C 118 (2014) 19450–19461, doi:10.1021/jp505651j.

[33] E. Gianotti, G. Berlier, K. Costabello, S. Coluccia, F. Meneau, *in-situ* synchrotron small-angle X-ray scattering study of MCM-41 crystallisation using gemini surfactants, Catal. Today 126 (2007) 203–210, doi:10.1016/j.cattod.2006.08.064.

[34] A.Y. Khodakov, V.L. Zholobenko, M. Impéror-Clerc, D. Durand, Characterization of the initial stages of SBA-15 synthesis by *in-situ* time-resolved small-angle X-ray scattering, J. Phys. Chem. B. 109 (2005) 22780–22790, doi:10.1021/jp052786z.

[35] K. Flodström, H. Wennerström, C.V. Teixeira, H. Amenitsch, M. Lindén, V. Alfredsson, Time-resolved *in-situ* studies of the formation of cubic mesoporous silica formed with triblock copolymers, Langmuir 20 (2004) 10311–10316, doi:10.1021/la0482958.

[36] K. Flodström, C.V. Teixeira, H. Amenitsch, V. Alfredsson, M. Lindén, *in-situ* synchrotron small-angle X-ray scattering/X-ray diffraction study of the formation of SBA-15 mesoporous silica, Langmuir 20 (2004) 4885–4891, doi:10.1021/la049637c.

[37] D. Baute, D. Goldfarb, Interaction of nitrates with pluronic micelles and their role in the phase formation of mesoporous materials, J. Phys. Chem. C. 111 (2007) 10931–10940, doi:10.1021/jp070886u.

[38] E. Leontidis, Hofmeister anion effects on surfactant self-assembly and the formation of mesoporous solids, Curr. Opin. Colloid Interface Sci. 7 (2002) 81–91.

[39] D. Zhao, Q. Huo, J. Feng, B.F. Chmelka, G.D. Stucky, Nonionic triblock and star diblock copolymer and oligomeric surfactant syntheses of highly ordered, hydrothermally stable, mesoporous silica structures, J. Am. Chem. Soc. 120 (1998) 6024–6036, doi:10.1021/ja974025i.

[40] Y. Ding, G. Yin, X. Liao, Z. Huang, X. Chen, Y. Yao, Key role of sodium silicate modulus in synthesis of mesoporous silica SBA-15 rods with controllable lengths and diameters, Mater. Lett. 75 (2012) 45–47, doi:10.1016/j.matlet.2012.01.091.

[41] P. Linton, J.C. Hernandez-Garrido, P.A. Midgley, H. Wennerström, V. Alfredsson, Morphology of SBA-15-directed by association processes and surface energies, Phys. Chem. Chem. Phys. 11 (2009) 10973–10982, doi:10.1039/b913755f.

[42] S. Bayati, L. Galantini, K.D. Knudsen, K. Schille, Effects of bile salt sodium glycodeoxycholate on the self-assembly of PEO–PPO–PEO triblock copolymer P123 in aqueous solution, Langmuir 31 (2015) 13519–13527, doi:10.1021/acs.langmuir.5b03828.

[43] S. Bayati, L. Galantini, K.D. Knudsen, K. Schillen, Complexes of PEO-PPO-PEO triblock copolymer P123 and bile salt sodium glycodeoxycholate in aqueous solution: a small angle x-ray and neutron scattering investigation, Colloids Surf. A Physicochem. Eng. Asp. 504 (2016) 426–436.

[44] B. Chu, Structure and dynamics of block copolymer colloids, Langmuir 11 (1995) 414–421, doi:10.1021/la00002a009.

[45] G. Wanka, H. Hoffmann, W. Ulbricht, Phase diagrams and aggregation behavior of triblock copolymers in aqueous solutions, Macromolecules 27 (1994) 4145–4159.

[46] L. Guo, R.H. Colby, M.Y. Lin, G.P. Dado, Micellar Structure Changes In Aqueous Mixtures Of Nonionic Surfactants, J. Rheol. 45 (2001), doi:10.1122/1.1389315.

[47] Z. Chen, T.L. Greaves, C. Fong, A. Caruso, C.J. Drummond, Lyotropic liquid crystalline phase behaviour in amphiphile – protic ionic liquid systems, Phys. Chem. Chem. Phys. 14 (2012) 3825–3836, doi:10.1039/c2cp23698b.

[48] S.S. Soni, G. Brotons, M. Bellour, T. Narayanan, A. Gibaud, Quantitative SAXS analysis of the P123/water/ethanol ternary phase diagram, J. Phys. Chem. B. 110 (2006) 15157–15165, doi:10.1021/jp062159p.

[49] T. Iwanaga, M. Suzuki, H. Kunieda, Effect of added salts or polyols on the liquid crystalline structures of polyoxyethylene-type nonionic surfactants, Langmuir (1998) 5775–5781.

[50] R.L. Baldwin, How Hofmeister interactions affect protein stability*, Biophys. J. 71 (1996) 2056–2063, doi:10.1016/S0006-3495(96)79404-3.

[51] A. Kabalnov, H. Wennerstrgm, Salt effects on nonionic microemulsions are driven by adsorption/depletion at the surfactant monolayer, J. Phys. Chem. (1995) 6220–6230.

[52] S. Manet, M. Imp, V. Zholobenko, D. Durand, C.L.P. Oliveira, J.S. Pedersen, I. Grillo, F. Meneau, C. Rochas, Structure of micelles of a nonionic block copolymer determined by SANS and SAXS, J. Phys. Chem. B. 115 (2011) 11318–11329.

[53] P. Taylor, B. Bharatiya, G. Ghosh, P. Bahadur, J. Mata, B. Bharatiya, G. Ghosh, P. Bahadur, J. Mata, The effects of salts and ionic surfactants on the micellar structure of tri-block copolymer PEO-PPO-PEO in aqueous solution, J. Dispers. Sci. Technol. 29 (2008) 696–701, doi:10.1080/01932690701751876.

[54] H. Lin, S. Liu, C. Mou, C. Tang, Hierarchical organization of mesoporous MCM-41 Ropes, Chem. Commun. (1999) 583–584.

[55] H. Lin, C. Kao, C. Mou, Counterion and alcohol effect in the formation of mesoporous silica, Microporous Mesoporous Mater. 48 (2001) 135–141.

[56] H. Lin, C. Kao, C. Mou, S. Liu, Counterion effect in acid synthesis of mesoporous silica materials, J. Phys. Chem. B. 104 (2000) 7885–7894.

[57] J.G. Croissant, Y. Fatieiev, A. Almalik, N.M. Khashab, Mesoporous silica and organosilica nanoparticles: physical chemistry, biosafety, delivery strategies, and biomedical applications, Adv. Healthc. Mater. 7 (1–75) (2018) 1700831, doi:10.1002/adhm.201700831.

[58] P. Linton, A.R. Rennie, V. Alfredsson, Evolution of structure and composition during the synthesis of mesoporous silica sba-15 studied by small-angle neutron scattering, Solid State Sci. 13 (2011) 793–799, doi:10.1016/j.solidstatesciences.2010.02.035.

[59] U. Bonse, M. Hart, Tailless X-ray single-crystal reflection curves obtained by multiple reflection, Appl. Phys. Lett. 7 (1965) 238–240, doi:10.1063/1.1754396.

[60] J. Ilavsky, F. Zhang, A.J. Allen, L.E. Levine, P.R. Jemian, G.G. Long, Ultra-small-angle X-ray scattering instrument at the advanced photon source: history, recent development, and current status, Metall. Mater. Trans. 44A (2013) 68–76, doi:10.1007/s11661-012-1431-y.

[61] M. Liu, G. Gadikota, Chemo-morphological coupling during serpentine heat treatment for carbon mineralization, Fuel 227 (2018) 379–385, doi:10.1016/j.fuel.2018.04.097.

[62] M. Liu, G. Gadikota, Phase evolution and textural changes during the direct conversion and storage of CO_2 to produce calcium carbonate from calcium hydroxide, Geosciences 8 (2018) 445, doi:10.3390/geosciences8120445.

[63] M. Liu, G. Gadikota, Probing the Influence of thermally induced structural changes on the microstructural evolution in shale using multiscale X-ray scattering measurements, Energy Fuels 32 (2018) 8193–8201, doi:10.1021/acs.energyfuels.8b01486.

[64] H. Asgar, S. Mohammed, I. Kuzmenko, G. Gadikota, Relating structural and microstructural evolution to the reactivity of cellulose and lignin during alkaline thermal treatment with $Ca(OH)_2$ for sustainable energy production integrated with CO_2 capture, ACS Sustain. Chem. Eng. 7 (2019) 5449–5461, doi:10.1021/acssuschemeng.8b06584.

[65] G. Gadikota, Connecting the morphological and crystal structural changes during the conversion of lithium hydroxide monohydrate to lithium carbonate using multi-scale X-ray scattering measurements, Minerals 7 (9) (2017) 169, doi:10.3390/min7090169.

[66] G. Gadikota, F. Zhang, A. Allen, In situ angstrom-to-micrometer characterization of the structural and microstructural changes in kaolinite on heating using ultrasmall-angle, small-angle, and wide-angle X-ray scattering, Ind. Eng. Chem. Res. (2017) 11791–11801, doi:10.1021/acs.iecr.7b02810.

[67] O. Glatter, O. Kratky, Small Angle X-ray Scattering, Academic Press, 1982.

[68] M. Nyam-Osor, D.V. Soloviov, Y.S. Kovalev, A. Zhigunov, A.V. Rogachev, O.I. Ivankov, R.V. Erhan, A.I. Kuklin, Silver behenate and silver stearate powders for calibration of SAS instruments, J. Phys. Conf. Ser. 351 (2012) 012024, doi:10.1088/1742-6596/351/1/012024.

[69] J. Ilavsky, Nika: software for two- dimensional data reduction, J. Appl. Crystallogr. 45 (2012) 324–326.

[70] J. Ilavsky, P.R. Jemian, Irena: tool suite for modeling and analysis of small-angle scattering, J. Appl. Crystallogr. 42 (2009) 347–353.

[71] M. Liu, H. Asgar, S. Seifert, G. Gadikota, Novel aqueous amine looping approach for the direct capture, conversion and storage of CO_2 to produce magnesium carbonate, Sustain. Energy Fuels 4 (2020) 1265–1275, doi:10.1039/c9se00316a.

[72] Q. Cheng, V. Pavlinek, C. Li, A. Lengalova, Y. He, P. Saha, Synthesis and characterization of new mesoporous material with conducting polypyrrole confined in mesoporous silica, Mater. Chem. Phys. 98 (2006) 504–508, doi:10.1016/j.matchemphys.2005.09.074.

[73] M.D. Alba, Z. Luan, J. Klinowski, Titanosilicate Mesoporous molecular sieve MCM-41: synthesis and characterization, J. Phys. Chem. 100 (1996) 2178–2182.

[74] M. Thommes, K. Kaneko, A.V. Neimark, J.P. Olivier, F. Rodrigues-Reinoso, J. Rouquerol, K.S.W. Sing, Physisorption of gases with special reference to the evaluation of surface area and pore size distribution (IUPAC technical report), Pure Appl. Chem. 87 (2015) 1051–1069.

[75] L. Cao, M. Kruk, Synthesis of large-pore SBA-15 silica from tetramethyl orthosilicate using triisopropylbenzene as micelle expander, Colloids Surfaces A Physicochem, Eng. Asp. 357 (2010) 91–96, doi:10.1016/j.colsurfa.2009.09.019.

[76] T. Kjellman, N. Reichhardt, M. Sakeye, J.H. Smaìštt, M. Lindén, V. Alfredsson, Independent fine-tuning of the intrawall porosity and primary mesoporosity of SBA-15, Chem. Mater. 25 (2013) 1989–1997, doi:10.1021/cm4009442.

[77] M.M. Mirhosseini, S.S. Zargarian, Fabrication and characterization of hydrophilic poly(e-caprolactone)/pluronic P123 electrospun fibers, J. Appl. Polym. Sci. 43345 (2016) 1–11, doi:10.1002/app.43345.

[78] G. Zhang, X. Chen, Y. Zhao, F. Ma, B. Jing, H. Qiu, Lyotropic liquid-crystalline phases formed by pluronic P123 in ethylammonium nitrate, J. Phys. Chem. B. 112 (2008) 6578–6584.

[79] R.M. Almeida, T.A. Guiton, C.G. Pantano, Detection of LO mode in vSIO2 by infrared diffuse reflectance spectroscopy, J. Non. Cryst. Solids. 119 (1990) 238–241.

[80] M. Muroya, Correlation between the formation of silica skeleton structure and Fourier transform reflection infrared absorption spectroscopy spectra, Colloids Surf., A 157 (1999) 147–155.

[81] M.C. Matos, L.M. Ilharco, R.M. Almeida, The evolution of teos to silica gel and glass by vibrational spectroscopy, J. Non Cryst. Solids 148 (1992) 232–237.

[82] D. Niznansky, J.L. Rehspringer, Infrared study of sol to gel evolution and gel aging, J. Non-Cryst. Solids 180 (1995) 191–196.

[83] V.A. Online, H. Song, Ag(I)-mediated self-assembly of anisotropic rods and plates in the surfactant mixture of CTAB and pluronics, RSC Adv. (2019) 4380–4389, doi:10.1039/C8RA10517K.

[84] G. Beaucage, Approximations leading to a unified exponential/power-law approach to small-angle scattering, J. Appl. Crystallogr. 28 (1995) 717–728.

[85] G. Beaucage, Small-angle scattering from polymeric mass fractals of arbitrary mass-fractal dimension, J. Appl. Crystallogr. 29 (1996) 134–146, doi:10.1107/S0021889895011605.

[86] S. Manet, M. Imp, V. Zholobenko, D. Durand, C.L.P. Oliveira, J.S. Pedersen, I. Grillo, F. Meneau, C. Rochas, Structure of micelles of a nonionic block copolymer determined by SANS and SAXS, J. Phys. Chem. B. 115 (2011) 11318–11329, doi:10.1021/jp200212g.

[87] R. Guillet-Nicolas, F. Bérubé, M. Thommes, M.T. Janicke, F. Kleitz, Selectively tuned pore condensation and hysteresis behavior in mesoporous SBA-15 silica: correlating material synthesis to advanced gas adsorption analysis, J. Phys. Chem. C. 121 (2017) 24505–24526, doi:10.1021/acs.jpcc.7b06745.

[88] P. Linton, A.R. Rennie, M. Zackrisson, V. Alfredsson, in-situ observation of the genesis of mesoporous silica SBA-15: dynamics on length scales from 1 nm to 1 μm, Langmuir 25 (2009) 4685–4691, doi:10.1021/la803543z.

[89] K.D.K. Im, G.B.K. Im, H.T.K. Im, Synthesis and characterization of mesoporous silica particles by sol-gel method: effect of aging time on surface area and pore size, J. Chem. Eng. Jpn. 38 (2005) 547–552.

[90] H.B.S. Chan, M. Budd, Control of mesostructured silica particle morphology, Mater. Chem. 11 (2001) 951–957, doi:10.1039/b005713o.

[91] N.P. Shusharina, S. Balijepalli, J.M. Gruenbauer, P. Alexandridis, Mean-field theory prediction of the phase behavior and phase structure of alkyl-propoxy-ethoxylate “graded” surfactants in water: temperature and electrolyte effects, Langmuir 19 (2003) 4483–4492, doi:10.1021/la026257n.

[92] S. Nagpure, S. Das, R.K. Garlapalli, J. Strzalka, S.E. Rankin, in-situ GISAXS investigation of low-temperature aging in oriented surfactant-mesostructured titania thin films, J. Phys. Chem. C 119 (2015) 22970–22984.

[93] M. Avrami, Kinetics of phase change. I: General theory, J. Chem. Phys. 7 (1939) 1103–1112.

[94] M. Avrami, Kinetics of phase change. II: Transformation-time relations for random distribution of nuclei, J. Chem. Phys. 8 (1940) 212–224.

[95] M. Avrami, Granulation, phase change, and microstructure kinetics of phase change, J. Chem. Phys. 9 (1941) 177–184.

[96] Z. Ding, J.E. Spruiell, Interpretation of the non-isothermal crystallization kinetics of polypropylene using a power law, J. Polym. Sci., Part B Polym. Phys. 35 (1997) 1077–1093.

[97] J.F. Toro-vazquez, E. Dibildox-alvarado, M. Charó-alonso, V. Herrera-coronado, C.A. Gómez-aldapa, The Avrami index and the fractal dimension in vegetable oil crystallization, JAOCS 79 (2002) 855–866, doi:10.1007/s11746-002-0570-y.